Research Square

Preprints are preliminary reports that have not undergone peer review.
They should not be considered conclusive, used to inform clinical practice,
or referenced by the media as validated information.

CRTAP is an oncogenic driver of extracellular matrix stiffening in glioblastoma

Devansh Swadia
Indian Institute of Science Education and Research Mohali https://orcid.org/0009-0002-2834-4676
Pritam Saha
Indian Institute of Science Education and Research Mohali
Sabyasachi Rakshit
srakshit@iisermohali.ac.in

Indian Institute of Science Education and Research Mohali

Research Article

Keywords: CRTAP, Glioblastoma, ECM, Stiffness, Collagen

Posted Date: November 24th, 2026

DOI: https://doi.org/10.21203/rs.3.rs-11841562/v1

License: This work is licensed under a Creative Commons Attribution 4.0 International License.
Read Full License

Additional Declarations: The authors declare no competing interests.

CRTAP is an oncogenic driver of extracellular matrix stiffening in glioblastoma

Devansh Swadia[1], Pritam Saha[1], Sabyasachi Rakshit[1]*

[1]Department of Chemical Sciences, Indian Institute of Science Education and Research Mohali, Sector 81, Knowledge City, S.A.S. Nagar, Punjab 140306, India.

*Corresponding author. Email: srakshit@iisermohali.ac.in

A collagen-modifying chaperone sets the mechanical state of the glioblastoma matrix and is targetable by AI-designed degraders.

Keywords: CRTAP, Glioblastoma, ECM, Stiffness, Collagen

Abstract

Glioblastoma (GBM) malignancy is governed by a stiff, remodeled extracellular matrix (ECM), yet the molecular architects of this mechanical niche remain undefined. We identify cartilage-associated protein (CRTAP), a component of the collagen prolyl 3-hydroxylation complex, as a regulator of GBM mechanobiology. In glioma cohorts and tissue microarrays, CRTAP expression rises with WHO grade, is enriched in isocitrate dehydrogenase (IDH) wild-type GBM and marks shorter overall survival at every grade. CRISPR-Cas9 disruption and genetic rescue show that CRTAP is required for proliferation, clonogenicity and three-dimensional spheroid invasion. CRTAP loss lowers collagen hydroxyproline content, disrupts fiber architecture, softens the matrix and reduces nuclear YAP. Using a generative AI chemistry pipeline we designed cereblon recruiting CRTAP-directed chimeras whose cytotoxicity depends on CRTAP expression. These findings define a CRTAP–collagen–YAP axis and a degradation strategy against ECM-driven therapeutic resistance.

INTRODUCTION

Glioblastoma (GBM) is the most aggressive primary malignancy of the adult central nervous system and remains associated with a median survival of approximately 12 to 15 months despite maximal surgical resection followed by radiotherapy and temozolomide (TMZ) chemotherapy (*1, 2*). Current classification integrates histology with molecular markers, most importantly IDH mutation and 1p/19q codeletion, which together define prognostically distinct entities (*3, 4*). The diffuse infiltrative nature of GBM, together with profound intratumoral and intertumoral heterogeneity, limits therapeutic efficacy and contributes to the near-universal recurrence of the disease. Although extensive genomic and transcriptomic profiling has identified recurrent molecular alterations that drive gliomagenesis (*5–8*), and single-cell studies have resolved the cellular states that underlie this heterogeneity (*9, 10*), these discoveries have translated into only modest clinical benefit, highlighting the need to investigate additional determinants of tumor progression.

Increasing evidence indicates that the extracellular matrix (ECM) is an active regulator of tumor biology rather than a passive structural scaffold (*11–14*). Compared with normal brain tissue, the GBM microenvironment exhibits extensive remodeling of ECM composition and architecture, accompanied by increased tissue stiffness and altered viscoelastic properties (*15, 16*). These biomechanical changes influence multiple aspects of tumor progression, including cell proliferation, invasion, stem-like behavior and therapeutic resistance; in glioma specifically, substrate rigidity governs cell morphology, motility and proliferation (*17*). Cells transduce such cues through adhesion- and cytoskeleton-dependent mechanisms that convert matrix mechanics into biochemical signals (*18–22*). In particular, the transcriptional co-activators YAP and TAZ integrate extracellular mechanical cues with gene expression programs that promote tumor growth and invasion (*23–26*). However, the molecular mechanisms responsible for generating and maintaining the mechanically altered ECM in glioblastoma remain poorly defined.

Collagen I is a principal structural determinant of ECM mechanics, and its organization depends on a series of highly regulated post-translational modifications that govern fibril assembly,

stability and mechanical integrity. Among these, prolyl 3-hydroxylation of the α1(I) Pro986 residue is mediated by an endoplasmic reticulum complex composed of CRTAP, prolyl 3-hydroxylase 1 (P3H1, also known as LEPRE1) and cyclophilin B. Loss-of-function mutations in CRTAP cause recessive osteogenesis imperfecta, in which defective collagen maturation compromises tissue architecture and mechanical strength (*27, 28*). In tumors, the best-characterized determinants of matrix mechanics are instead the lysyl oxidase (LOX)-dependent covalent crosslinks that stiffen collagen and potentiate integrin signaling, invasion and metastatic colonization (*29, 30*), together with the tensional and architectural changes that accompany malignant transformation (*31–35*). Whether the collagen prolyl 3-hydroxylation machinery — which acts earlier, on the quality of the collagen molecule itself — contributes to pathological ECM remodeling in cancer has not been established. Although transcript- and antibody-level surveys catalog CRTAP across tumor types, to our knowledge CRTAP has not previously been investigated functionally in any malignancy.

Here, we investigated the role of CRTAP in regulating the biomechanical properties of the glioblastoma microenvironment. Integrating transcriptomic analyses of patient cohorts with CRISPR-Cas9-mediated gene disruption, functional cellular assays, collagen organization studies and biophysical measurements of matrix mechanics, we show that CRTAP promotes collagen hydroxylation, matrix assembly and ECM stiffening in GBM, and that its loss attenuates YAP nuclear localization while suppressing proliferation, clonogenicity and invasion. To connect this biophysical mechanism to a therapeutic strategy, we then applied a generative design pipeline to construct chimeric molecules that pair a CRTAP-directed fragment with the cereblon ligand thalidomide, following the proteolysis-targeting chimera (PROTAC) paradigm (*36, 37*) that exploits cereblon as the thalidomide receptor (*38*) and building on the broader use of machine learning in small-molecule discovery (*39, 40*). These findings identify CRTAP as a previously unrecognized regulator of glioblastoma mechanobiology and provide evidence that collagen post-translational modification contributes to the establishment of a tumor-supportive mechanical microenvironment.

RESULTS

CRTAP expression rises with glioma grade and tracks with aggressive molecular subtypes

To determine whether CRTAP is linked to glioma malignancy, we first examined its transcript levels in the Chinese Glioma Genome Atlas (CGGA) RNA-sequencing cohort (*41*). Across histological subtypes, CRTAP expression differed significantly ($P = 1.9 \times 10^{-6}$; Fig. 1A). Primary oligodendroglioma had the lowest expression (median $\log_2$ expression, 3.7), followed by astrocytoma, anaplastic oligodendroglioma and anaplastic astrocytoma. Glioblastoma had the highest median expression and the widest spread, with individual tumors reaching approximately 5.2. Recurrent tumors showed the same pattern: recurrent oligodendroglioma, recurrent astrocytoma, recurrent anaplastic astrocytoma and recurrent GBM each had higher median CRTAP expression than the corresponding primary low-grade tumor, suggesting that CRTAP expression is retained or gained as the disease progresses. Anaplastic astrocytoma and recurrent anaplastic astrocytoma spanned a wide range of expression, pointing to biological heterogeneity within intermediate-grade astrocytic tumors.

When tumors were grouped by WHO grade, CRTAP expression rose stepwise with grade ($P = 2.8 \times 10^{-8}$; Fig. 1B): median expression was lowest in grade II, intermediate in grade III and highest in grade IV. Because WHO CNS classification now relies on molecular features (*4*), we next stratified the cohort by IDH mutation and 1p/19q codeletion status. IDH-wild-type gliomas expressed significantly more CRTAP than IDH-mutant tumors (median, 4.2 versus 3.9; Fig. 1C) and expression was more variable in the IDH-wild-type group. Likewise, 1p/19q non-codeleted tumors had higher CRTAP expression than 1p/19q-codeleted tumors ($P = 5.1 \times 10^{-7}$; Fig. 1D). Because 1p/19q codeletion defines oligodendroglioma, the glioma subtype with the most favorable prognosis, these data link low CRTAP expression to a favorable molecular background.

To combine these markers, we analyzed CRTAP across five integrated molecular subgroups (Fig. 1E). Expression differed most strongly in this analysis ($P = 4.2 \times 10^{-10}$). IDH-mutant, 1p/19q-codeleted lower-grade glioma (LGG) had the lowest expression; IDH-mutant, 1p/19q non-codeleted LGG and IDH-wild-type LGG were intermediate, with the IDH-wild-type LGG group showing a particularly broad distribution consistent with a molecularly high-risk subset. IDH-mutant GBM had relatively low expression, similar to IDH-mutant LGG, whereas IDH-wild-type GBM had the highest expression of any subgroup. Together, these results show that CRTAP upregulation tracks primarily with IDH-wild-type status rather than with histological

grade alone, and is greatest in IDH-wild-type GBM, the most aggressive and treatment-resistant glioma entity.

To corroborate the transcriptomic findings experimentally, we measured CRTAP mRNA by quantitative reverse transcription polymerase chain reaction (RT-qPCR) in the human GBM cell line U87MG and in non-transformed NIH3T3 fibroblasts (Fig. 1F). U87MG cells had markedly higher CRTAP transcript levels (median relative expression, 11-fold versus 1.5-fold in NIH3T3), corresponding to an approximately seven- to eightfold enrichment. Finally, we asked whether the transcript-level findings hold at the protein level in patient tissue. We performed immunohistochemistry on commercially available glioma tissue microarrays containing normal brain, low-grade glioma (LGG), high-grade glioma (HGG) and GBM cores (Fig. 1G). Normal brain tissue showed the lowest CRTAP signal, with hematoxylin-counterstained nuclei visible and little detectable 3,3′-diaminobenzidine (DAB) staining. LGG showed moderate, diffuse cytoplasmic CRTAP staining across the tumor parenchyma. HGG showed strong, dense cytoplasmic staining together with prominent nuclear positivity in many tumor cells. GBM had the most intense and widespread immunoreactivity, with strong nuclear and cytoplasmic CRTAP staining in densely packed tumor cells surrounding a central vascular or necrotic-appearing region, which itself stained only weakly. Staining intensity and the proportion of positive cells therefore rose progressively from normal brain to LGG, HGG and GBM, mirroring the grade-dependent pattern seen in the CGGA transcriptome. Taken together, data from three independent levels of evidence including patient transcriptomes, cell lines and patient tissue show that CRTAP is upregulated in glioma, rises with tumor grade and is most enriched in IDH-wild-type glioblastoma, identifying CRTAP as a candidate marker of glioma aggressiveness.

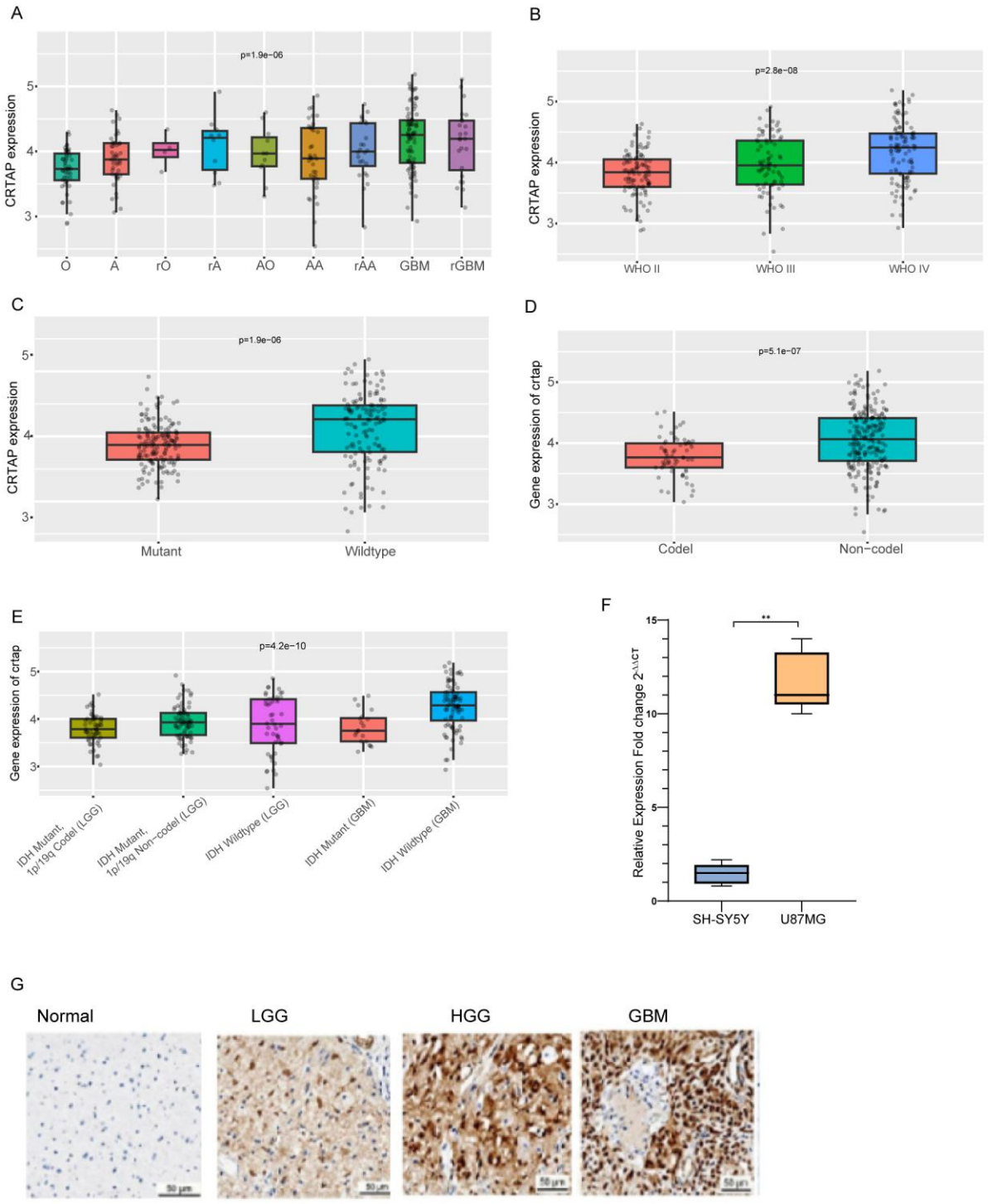

Fig. 1. CRTAP is upregulated in glioma and increases with tumor grade and aggressive molecular subtypes. (**A**) CRTAP mRNA expression in the CGGA RNA-seq cohort by histological subtype: oligodendroglioma (O), astrocytoma (A), recurrent oligodendroglioma

(rO), recurrent astrocytoma (rA), anaplastic oligodendroglioma (AO), anaplastic astrocytoma (AA), recurrent anaplastic astrocytoma (rAA), glioblastoma (GBM) and recurrent glioblastoma (rGBM). (**B**) CRTAP expression by WHO grade (II, III and IV). (**C**) CRTAP expression in IDH-mutant versus IDH-wild-type gliomas. (**D**) CRTAP expression in 1p/19q-codeleted versus non-codeleted gliomas. (**E**) CRTAP expression across integrated molecular subgroups: IDH-mutant 1p/19q-codeleted LGG, IDH-mutant 1p/19q non-codeleted LGG, IDH-wild-type LGG, IDH-mutant GBM and IDH-wild-type GBM. In (A) to (E), expression is shown as $\log_2(\text{FPKM} + 1)$. Boxes show the median and interquartile range, whiskers span the 10th to 90th percentiles, and each dot is one patient; P values are from the Kruskal–Wallis test for multi-group comparisons and the Mann–Whitney U test for two-group comparisons. (**F**) RT-qPCR of CRTAP mRNA in NIH3T3 and U87MG cells, shown as fold change ($2^{-\Delta\Delta C_{-}\{T\}}$) normalized to GAPDH; n = 3 independent experiments. (**G**) Representative CRTAP immunohistochemistry on glioma tissue microarrays showing normal brain, low-grade glioma (LGG), high-grade glioma (HGG) and GBM cores. DAB (brown), hematoxylin counterstain (blue). Scale bars, 50 μm.

High CRTAP expression predicts poor overall survival in glioma at every WHO grade

Because CRTAP expression rose with tumor grade and was enriched in molecularly aggressive subtypes, we next asked whether it carries prognostic information. Patients in the CGGA cohort with available survival data (n = 222) were split into CRTAP-high and CRTAP-low groups at the median expression value. Overall survival (OS) was compared by Kaplan–Meier analysis with the log-rank test, first within each WHO grade and then across the whole cohort (Fig. 2, A to D).

In WHO grade II glioma (n = 90; 45 high, 45 low), high CRTAP expression was associated with significantly shorter OS (P = 0.033; Fig. 2A). The curves began to separate within approximately the first 500 days. By about 1100 days, roughly 80% of CRTAP-high patients were still alive, compared with almost all CRTAP-low patients. Median OS in the CRTAP-high group was about 3250 days and was not reached in the CRTAP-low group, whose survival plateaued at about 69% from roughly 3500 days onward; the CRTAP-high group plateaued at about 47%. Thus, even among low-grade tumors, which usually progress slowly, high CRTAP expression identifies patients with a clearly worse long-term outcome.

The prognostic effect was more pronounced in WHO grade III glioma (n = 47; 24 high, 23 low; P = 0.0054; Fig. 2B). The two curves overlapped during the first 800 days and then separated sharply. CRTAP-high patients had a median OS of about 1000 days; their survival fell to about 14% by 1650 days and to 0% by 3700 days, leaving no long-term survivors in this group. In contrast, the CRTAP-low group plateaued at about 52% from 1250 days onward and median OS was not reached during follow-up. In anaplastic glioma, therefore, CRTAP expression separates patients with durable long-term survival from those whose disease is uniformly fatal.

High CRTAP expression also predicted a worse outcome in WHO grade IV glioblastoma (n = 85; 43 high, 42 low; P = 0.013; Fig. 2C), the most aggressive group. Median OS was about 380 days for CRTAP-high patients and about 600 days for CRTAP-low patients, an absolute difference of roughly 7 months. Survival in the CRTAP-high group dropped steeply to about 5% by approximately 1100 days, whereas about 40% of CRTAP-low patients were still alive at 800 days and a small fraction of long-term survivors remained beyond 2400 days. That GBM can be further stratified by prognosis using a single transcript is notable, because survival is uniformly poor in this group.

Finally, in the full cohort across all grades (n = 222; 111 high, 111 low), high CRTAP expression was strongly associated with shorter OS ($P < 0.0001$; Fig. 2D). Median OS was about 860 days in the CRTAP-high group and about 3150 days in the CRTAP-low group, a nearly fourfold difference. The curves separated within the first year and continued to diverge over follow-up, with long-term survival plateauing at about 45% in CRTAP-low patients compared with about 17% in CRTAP-high patients. Taken together, these data show that high CRTAP expression consistently predicts poor overall survival in glioma, both across the whole cohort and within each WHO grade. Because grade-stratified analysis yields the same result, CRTAP carries prognostic information that is not simply a restatement of histological grade; formal multivariable testing against age, grade and IDH status will be required to establish independence.

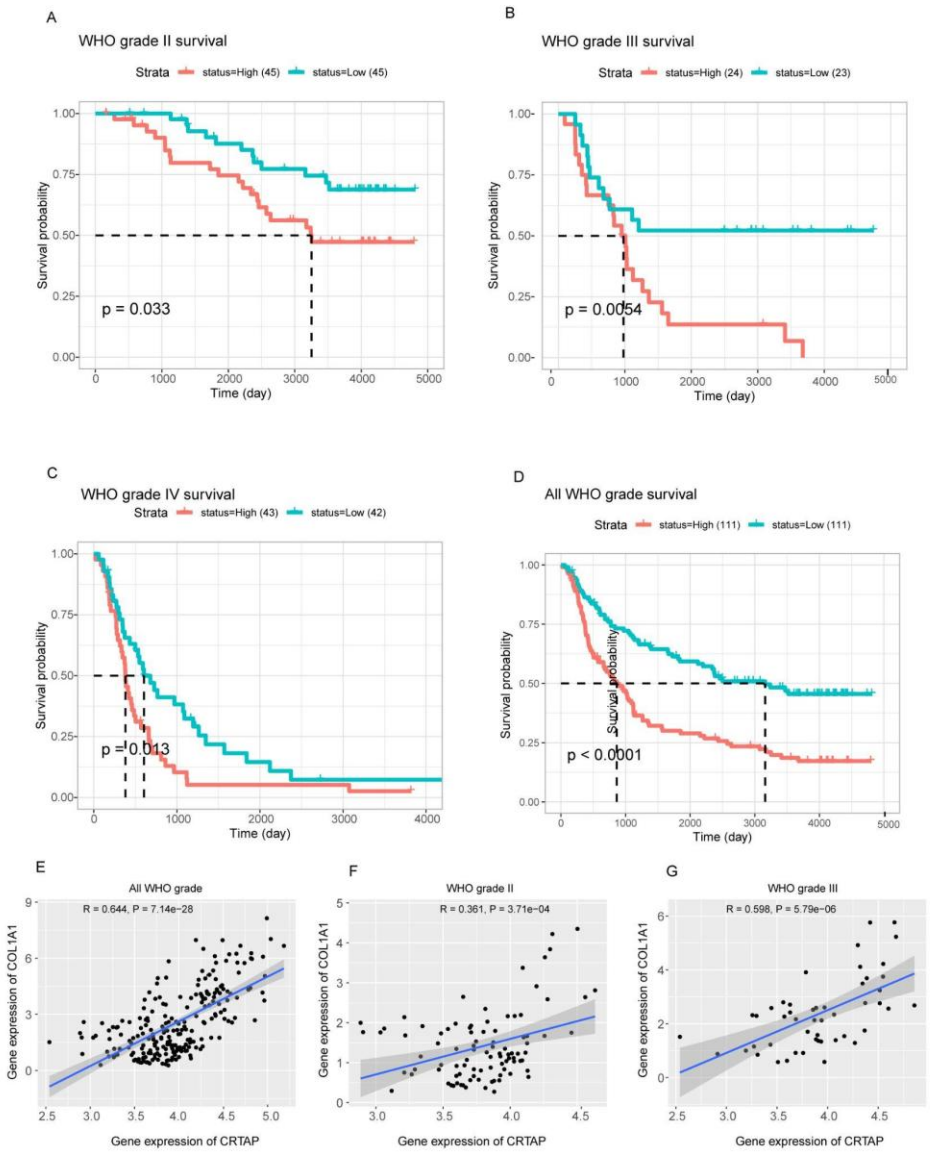

Fig. 2. High CRTAP expression predicts poor overall survival in glioma patients. Kaplan–Meier overall survival curves for CGGA glioma patients split into CRTAP-high (red) and CRTAP-low (cyan) groups at the median expression value. (**A**) WHO grade II (high, n = 45; low, n = 45; P = 0.033). (**B**) WHO grade III (high, n = 24; low, n = 23; P = 0.0054). (**C**) WHO grade IV (high, n = 43; low, n = 42; P = 0.013). (**D**) All WHO grades combined (high, n = 111; low, n = 111; P < 0.0001). Dashed lines mark median survival; vertical ticks mark censored patients. Time is in days. P values were calculated by the two-sided log-rank test.

CRISPR knockout of CRTAP reduces glioblastoma cell proliferation, clonogenicity and invasion

To test whether CRTAP is functionally required in GBM cells, we generated CRTAP-knockout (KO) U87MG cells by CRISPR-Cas9 genome editing and reconstituted them with CRTAP complementary DNA (rescue). RT-qPCR confirmed efficient depletion and successful restoration of CRTAP (Fig. 3A). Relative to wild-type (WT) cells (median fold change, 12.9), CRTAP transcript levels in KO cells fell by about 80% (median, ≈2.5; $P < 0.001$). Re-expression restored CRTAP to a median of 10, significantly higher than in KO cells ($P < 0.001$) and not significantly different from WT; the rescue line therefore reached roughly 75 to 80% of endogenous CRTAP expression.

We first measured proliferation by MTT assay over 120 hours (Fig. 3B). WT cells grew steadily, with absorbance at 570 nm (OD_{570}) rising from 24 to 120 hours to reach approximately 0.50. CRTAP-KO cells grew markedly more slowly at every time point, reaching only 0.19 at 120 hours, a 62% reduction relative to WT at the endpoint ($P < 0.01$). Re-expressing CRTAP largely restored proliferation: the rescue growth curve ran almost parallel to the WT curve, and at 120 hours rescue cells grew significantly more than KO cells ($P < 0.01$) and did not differ significantly from WT cells.

To test long-term survival and self-renewal capacity, we performed clonogenic assays (Fig. 3, C and D). WT cells formed numerous large, dense, intensely crystal violet-stained colonies, whereas CRTAP-KO cells formed only a few small, scattered colonies, many of them at or below the size threshold (Fig. 3C). Quantification showed that CRTAP loss reduced colony number by about 74%, from a median of 120 colonies in WT cells to 31 in KO cells ($P < 0.001$; Fig. 3D). Re-expressing CRTAP fully restored colony-forming ability (median, 130), significantly more than KO ($P < 0.001$) and not different from WT.

Finally, we assessed the invasive ability of 3D tumor spheroids over 72 hours (Fig. 3, E and F). WT spheroids showed extensive invasion into the surrounding matrix, with radial, finger-like protrusions and single cells spreading from a dense core (Fig. 3E). CRTAP-KO spheroids remained compact and nearly spherical, with a smooth border and only short, sparse protrusions.

Rescue spheroids regained an invasive phenotype, with an irregular leading edge and clusters of cells budding into the matrix. Quantification of the invaded area matched these observations (Fig. 3F): between 24 and 72 hours, KO spheroids expanded by only about 11,000 μm^2, compared with about 34,000 μm^2 for WT, and rescue spheroids invaded in a pattern close to WT, significantly exceeding KO spheroids at 72 hours ($P < 0.001$).

Taken together, these loss- and gain-of-function experiments show that CRTAP is required for GBM cell proliferation, clonogenic survival and three-dimensional invasion. Re-expressing CRTAP reversed all three defects, indicating that the phenotypes are caused specifically by CRTAP loss rather than by off-target editing, and providing a functional explanation for the association between high CRTAP expression and aggressive disease in patients.

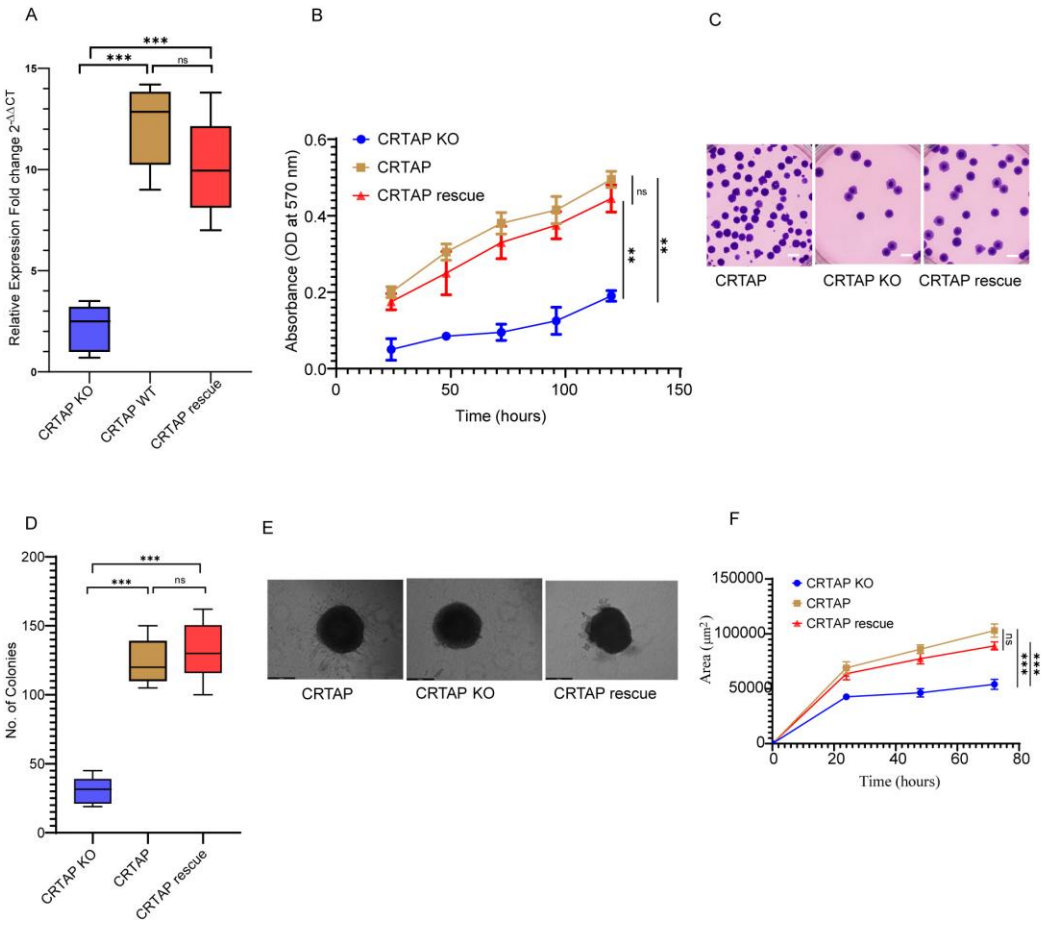

Fig. 3. CRTAP knockout impairs glioblastoma cell proliferation, clonogenicity and 3D invasion, and re-expression of CRTAP rescues these defects. (**A**) RT-qPCR of CRTAP mRNA in U87MG CRTAP-knockout (KO), wild-type (WT) and CRTAP-rescue cells, shown as fold change ($2^{-\Delta\Delta C_{-}\{T\}}$) normalized to GAPDH. (**B**) MTT proliferation assay of CRTAP KO (blue), CRTAP WT (brown) and CRTAP rescue (red) cells at 24, 48, 72, 96 and 120 hours, shown as absorbance at 570 nm; statistics are for the 120-hour time point. (**C**) Representative crystal violet-stained wells from the clonogenic assay for CRTAP WT, KO and rescue cells. (**D**) Number of colonies in the clonogenic assay shown in (C). (**E**) Representative bright-field images of 3D tumor spheroids from CRTAP WT, KO and rescue cells after 72 hours of invasion. (**F**) Spheroid invaded area (μm^2) quantified at 0, 24, 48 and 72 hours; statistics are for the 72-hour time point. Data are from three independent experiments; **P < 0.01,** *P < 0.001 by two-way (B and F) or one-way (A and D) analysis of variance (ANOVA) with Tukey's post hoc test; ns, not significant.

CRTAP regulates collagen hydroxylation, matrix architecture and ECM stiffness

Because CRTAP is a component of the collagen prolyl 3-hydroxylation complex (*27*), we asked whether its loss alters the composition and mechanics of the matrix deposited by GBM cells. Collagen was purified from ascorbate-stimulated cultures of parental U87MG, CRTAP-KO and CRTAP-rescue cells, and hydroxyproline content was quantified colorimetrically. Wild-type cultures maintained a high baseline concentration (1.7 μg/ml), knockout of CRTAP caused a marked reduction (0.5 μg/ml; $P < 0.001$), and genetic rescue restored hydroxyproline to wild-type levels (1.4 μg/ml; $P < 0.001$ versus KO; Fig. 4A).

To evaluate the structural consequences of CRTAP loss on matrix organization, we performed Masson's trichrome staining (Fig. 4E). Wild-type cultures exhibited a dense, continuous and highly organized collagen network with robust blue staining along the fibrous matrix. In contrast, CRTAP-deficient cells showed severe matrix disruption, characterized by a near-complete absence of stained collagen fibers and sparse ECM density. Re-expression of CRTAP restored collagen bundle alignment and architecture to levels indistinguishable from wild-type controls. Morphometric quantification of the collagen area fraction by color deconvolution (*42*) confirmed

this impression (Fig. 4F): the collagen area fraction fell from approximately 74% in wild-type cultures to approximately 5% in CRTAP-KO cultures ($P < 0.001$) and returned to approximately 73% upon rescue ($P < 0.001$ versus KO; not significant versus WT).

Given that collagen content and hydroxylation are key determinants of biomechanical properties, we next measured the micromechanical stiffness of the cell-derived matrix using a custom magnetic tweezers platform (Fig. 4B). Real-time tracking of bead displacement under magnetic actuation, analyzed by step-fitting, captured dynamic matrix stiffness profiles (Fig. 4D). Wild-type U87MG cultures were the most rigid (median stiffness, ≈26), stiffness dropped significantly in the absence of CRTAP (median, ≈15; $P < 0.01$), and re-expression of CRTAP significantly restored matrix rigidity (median, ≈22; $P < 0.01$ versus KO; Fig. 4C). Together, these data establish that CRTAP-dependent collagen modification is required for the assembly and mechanical integrity of the tumor-derived matrix.

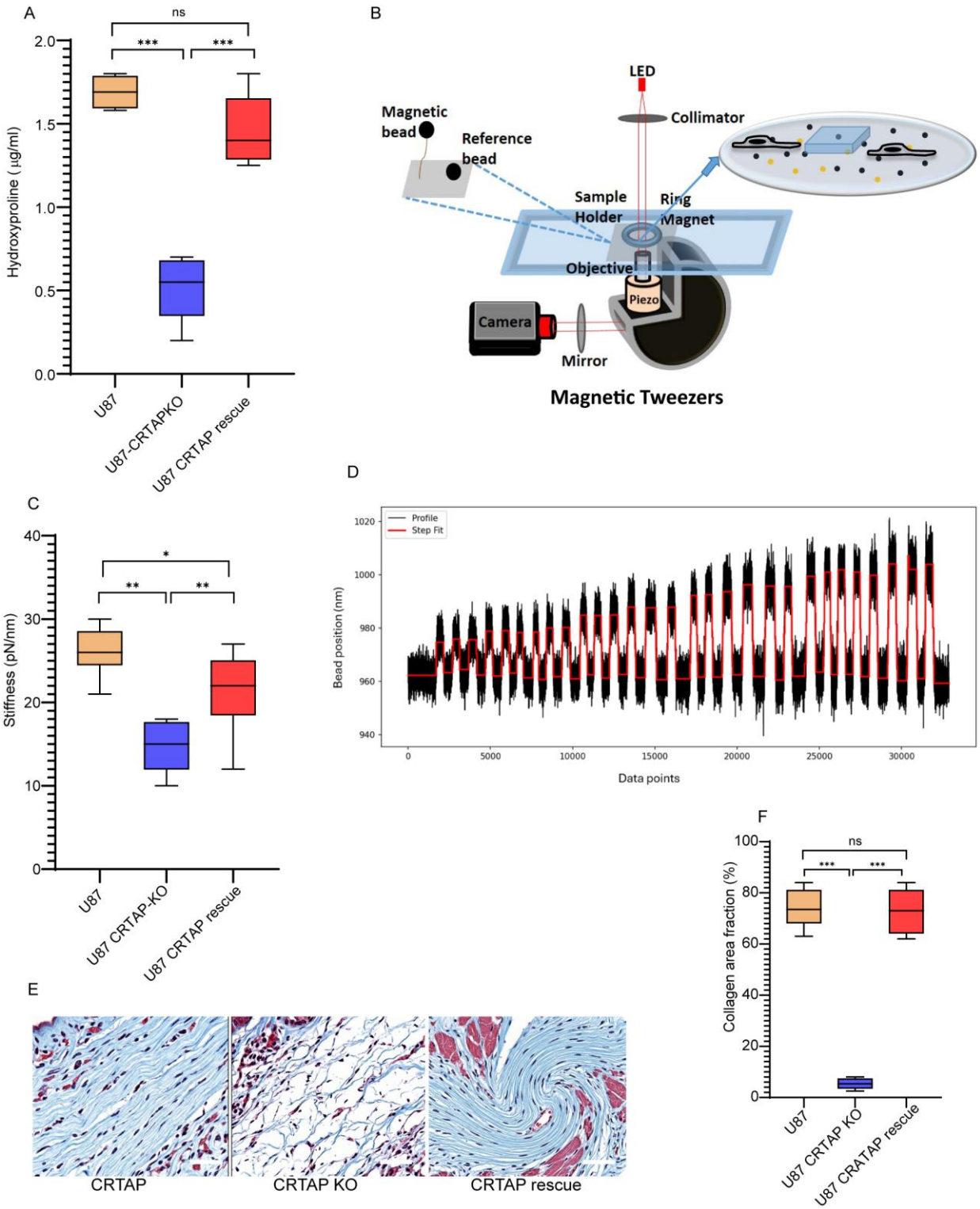
A
ns
***
***
Hydroxyproline (µg/ml)
2.0
1.5
1.0
0.5
0.0
U87
U87-CRTAPKO
U87 CRTAP rescue
B
LED
Collimator
Magnetic bead
Reference bead
Sample Holder
Ring Magnet
Objective
Piezo
Camera
Mirror
Magnetic Tweezers
C
*
**
**
Stiffness (pN/nm)
40
30
20
10
0
U87
U87 CRTAP-KO
U87 CRTAP rescue
D
Profile
Step Fit
Bead position (nm)
1020
1000
980
960
940
0
5000
10000
15000
20000
25000
30000
Data points
E
CRTAP
CRTAP KO
CRTAP rescue
F
ns
***
***
Collagen area fraction (%)
100
80
60
40
20
0
U87
U87 CRTAP KO
U87 CRATAP rescue

Fig. 4. CRTAP regulates collagen hydroxylation, matrix assembly and stiffness in glioma cells. (**A**) Hydroxyproline content measured by colorimetric assay in collagen purified from parental U87MG, CRTAP-knockout (U87-CRTAP KO) and CRTAP-rescue (U87 CRTAP rescue) cultures. (**B**) Schematic of the custom magnetic tweezers platform used for micromechanical measurements. (**C**) Matrix stiffness (pN/nm) measured by magnetic tweezers on cells secreted ECM using Z extension of 2.4 μm magnetic beads with n=25 beads and n=3 coverslip per condition. (**D**) Representative single-bead tracking profile (black) and step-fit model (red) recording bead displacement (nm) under magnetic force actuation over time. (**E**) Masson's trichrome staining showing collagen fiber architecture (blue) and cellular components (red/purple) across conditions. Scale bar, 50 μm. (**F**) Morphometric quantification of the collagen area fraction (%) derived from the Masson's trichrome images in (E). Data are from three independent experiments; $P < 0.05$, $P < 0.01$, **$P < 0.001$ by one-way ANOVA with Tukey's post hoc test; ns, not significant.

CRTAP loss disrupts YAP mechanosignaling

Matrix stiffness is transduced into transcriptional output largely through nuclear translocation of YAP (*23, 26*). Because CRTAP loss softened the matrix, we asked whether it also altered YAP localization. We performed immunofluorescence confocal microscopy in CRTAP WT and CRTAP KO cells (Fig. 5A). Control cells showed predominant nuclear compartmentalization of the YAP signal (red), with clear overlap with DAPI-stained nuclei (cyan). CRTAP deletion markedly disrupted this distribution, resulting in a pronounced loss of nuclear signal intensity alongside diminished overall cellular fluorescence. Quantitative morphometry confirmed a significant shift in intracellular localization (Fig. 5B): control cells displayed a median nuclear-to-cytoplasmic (N/C) ratio of 0.55, whereas CRTAP knockout reduced the N/C ratio to 0.18 ($P < 0.001$). CRTAP expression is therefore required for efficient nuclear accumulation of YAP, placing CRTAP-dependent matrix stiffening upstream of YAP mechanotransduction in GBM cells.

To characterize the transcriptional programs associated with CRTAP more broadly, we ranked all genes by their correlation with CRTAP expression in the TCGA-GBM cohort using GEPIA2

(*44*) and performed Gene Set Enrichment Analysis across the three Gene Ontology (GO) domains with clusterProfiler (*45*). In the biological process domain (Fig. 5C), the only terms reaching statistical significance (FDR $\leq$ 0.05) were endoderm development and bone development, both positively enriched. Additional positively correlated terms that did not reach the significance threshold included ossification, extracellular structure organization, actin filament organization, wound healing and collagen metabolic process, whereas negatively correlated terms were dominated by regulatory and immune-associated networks, including canonical NF-κB signal transduction, cytokine-mediated signaling and regulation of innate immune response.

In alignment with the molecular function of CRTAP in collagen folding and modification, cellular component analysis revealed significant positive enrichment (FDR $\leq$ 0.05) for the collagen trimer, the collagen-rich extracellular matrix and the endoplasmic reticulum lumen (Fig. 5D); distal axon, protein complex involved in cell adhesion and Golgi lumen showed positive but non-significant trends, and nuclear envelope, preribosome and nuclear speck showed negative enrichment scores. Molecular function analysis identified extracellular matrix structural constituent as the top significantly enriched category (FDR $\leq$ 0.05; Fig. 5E), with positive but non-significant trends spanning isomerase activity, collagen binding, SMAD binding, fibronectin binding, integrin binding and dioxygenase activity. Cysteine-type peptidase activity was the only significantly suppressed molecular function (FDR $\leq$ 0.05). The convergence of the significantly enriched terms on collagen assembly, the endoplasmic reticulum lumen and ECM structural constituents provides orthogonal, patient-derived support for the biochemical and biophysical phenotypes described above.

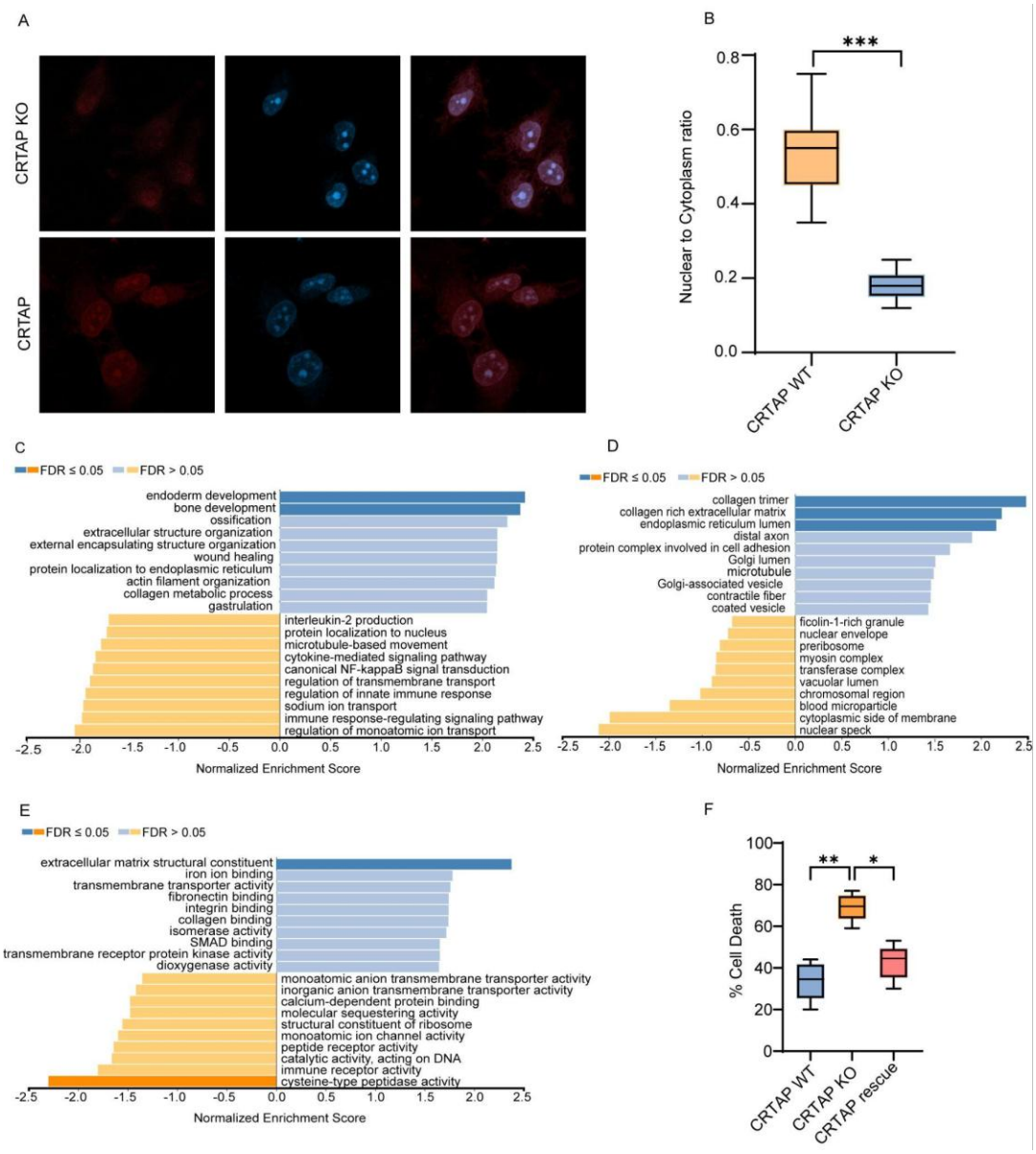

Fig. 5. CRTAP expression is required for nuclear YAP localization and correlates with extracellular matrix programs in patient tumors. (**A**) Representative immunofluorescence confocal images showing YAP distribution (red), nuclear counterstain (DAPI, cyan) and merged channels in CRTAP wild-type (CRTAP WT) and knockout (CRTAP KO) U87MG cells. Scale bar, 20 μm. (**B**) Quantification of the nuclear-to-cytoplasmic fluorescence intensity ratio in CRTAP WT versus CRTAP KO cells. Data are presented as box-and-whisker plots depicting the median, interquartile range and minimum-to-maximum whiskers; *P < 0.001 by two-tailed unpaired Student's t test (**C to E**) Gene Ontology Gene Set Enrichment Analysis of genes ranked by their correlation with CRTAP expression in the TCGA-GBM cohort, shown for (**C**)

Biological Process, (**D**) Cellular Component and (E) Molecular Function. Bar lengths indicate the normalized enrichment score; dark blue and orange bars denote terms with FDR ≤ 0.05, pale bars denote FDR > 0.05. Significance was determined using Benjamini–Hochberg-adjusted P values. (**F**) Quantification of temozolomide-induced cytotoxicity (% Cell Death) across wild-type (CRTAP WT), CRTAP-knockout (CRTAP KO), and CRTAP-rescued (CRTAP rescue) cells treated with temozolomide for 24 hours, as determined by Annexin V-FITC and propidium iodide (PI) dual-staining flow cytometry (Thermo Fisher Scientific, catalog no. V13242; BD FACSAria). Total % Cell Death represents the sum of early apoptotic (Annexin V^+/PI^-), late apoptotic (Annexin V^+/PI^+), and necrotic (Annexin V^-/PI^+) cell fractions. Data are represented as box-and-whisker plots showing the median (horizontal line), interquartile range (25th to 75th percentiles, box), and minimum-to-maximum values (whiskers) from [n = 3] independent biological replicates. Statistical significance was determined by one-way analysis of variance (ANOVA) followed by Tukey's multiple comparisons test ($* P < 0.05, ** P < 0.01$).

Generative design and evaluation of CRTAP-directed chimeras

Having established CRTAP as a functionally required regulator of GBM matrix mechanics, we asked whether it is chemically tractable. We built an automated computer-aided design pipeline in RDKit (*46*) to join a cereblon-binding thalidomide anchor to a CRTAP-directed fragment through a flexible linker (Fig. 6A). A stochastic genetic algorithm generated 500 linker configurations, and filtering against Lipinski criteria, RDKit valency sanitization and a molecular weight ceiling of 1200 Da eliminated structurally unstable configurations, yielding a refined structural library. Ranking by the quantitative estimate of drug-likeness (QED) (*47*) identified CRTAP-PROTAC-AI-4 as the leading candidate (QED, 0.520; molecular weight, 489.25 Da), with CRTAP-PROTAC-AI-53 (QED, 0.503; 491.23 Da) and CRTAP-PROTAC-AI-45 (QED, 0.484; 503.26 Da) as the second- and third-ranked candidates (Fig. 6, B to D) (Table 1). Molecular docking with CB-Dock2 (*48*) predicted favorable binding conformations and identified Cys112, Glu82, Thr95 and Val108 as key contact residues between the CRTAP-thalidomide construct and its target pocket (Fig. 6E).

To determine whether the cereblon anchor itself engages CRTAP, real-time binding kinetics were characterized by bio-layer interferometry (BLI). Recombinant CRTAP (≈47 kDa) was covalently immobilized on amine-reactive second-generation (AR2G) biosensor tips as the capture ligand, establishing a stable baseline for measuring association and dissociation of thalidomide (molecular weight ≈ 258 Da). Immobilized CRTAP biosensors exposed to increasing concentrations of thalidomide (9.375 to 300 nM) displayed concentration-dependent association responses over the 300-s binding phase (Fig. 6F). Upon transfer into analyte-free buffer, dissociation was recorded over 600 s, demonstrating reversible binding. Global fitting of the double-referenced kinetic profiles to a 1:1 Langmuir interaction model yielded an association rate constant (k_a) of 1.25×10^5 M^{-1} s^{-1} and a dissociation rate constant (k_d) of 4.50×10^{-3} s^{-1}, giving an equilibrium dissociation constant ($K_D = k_d/k_a$) of 36 nM. The theoretical global fit showed strong concordance with the experimental data ($R^2 = 0.994$; reduced $\chi^2 = 0.012$). These parameters indicate a high-affinity interaction between thalidomide and CRTAP, driven by a rapid association rate and a stable complex.

Finally, to evaluate whether chimera-induced cell death depends on CRTAP expression, we quantified cell death by flow cytometry in U87MG cells after treatment with the thalidomide-based construct (Fig. 6G). Wild-type U87MG cells showed robust cell death (>80%), whereas CRTAP-knockout cells showed significantly less cell death (<40%; $P < 0.01$), consistent with target-dependent cytotoxicity.

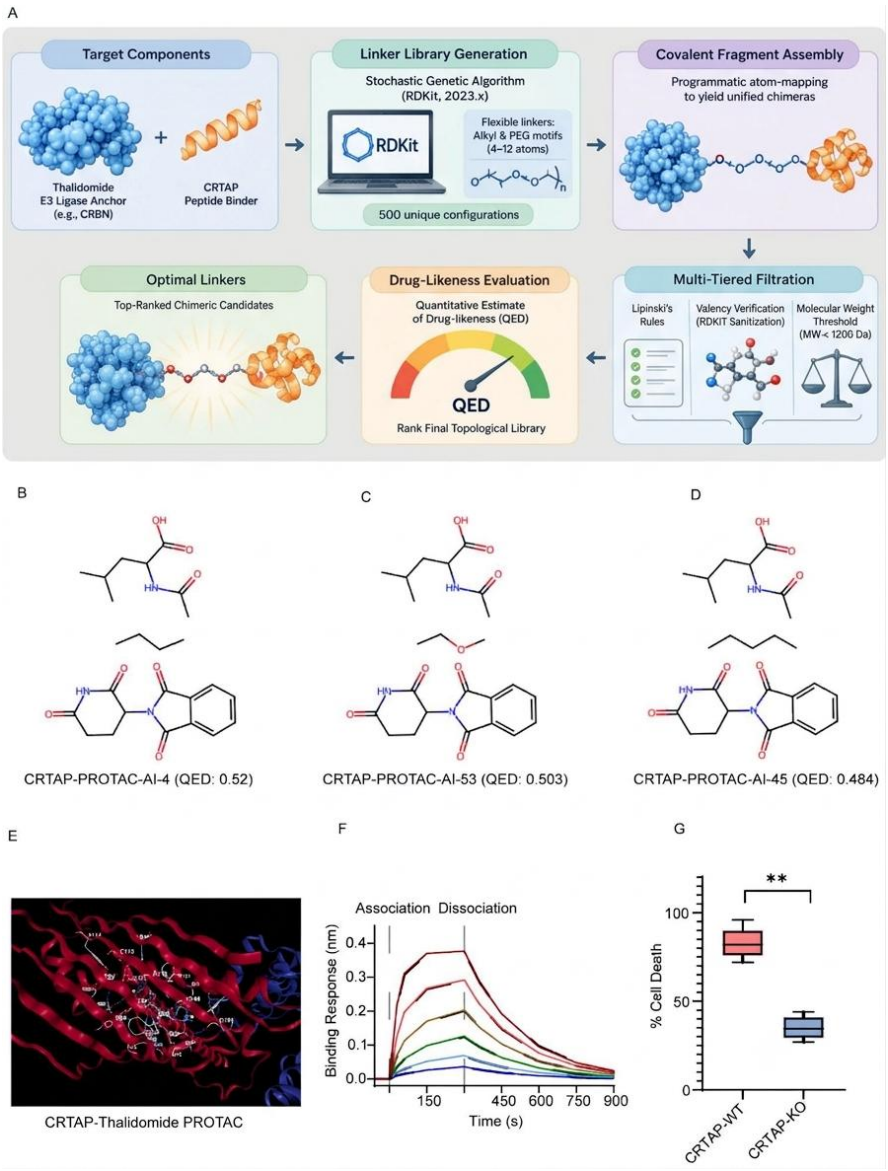

Fig. 6. Generative design, molecular modeling and functional evaluation of CRTAP-directed chimeras. (**A**) Schematic of the computational pipeline for CRTAP-directed chimera development, illustrating target components, linker library generation via a stochastic genetic algorithm (RDKit), fragment assembly, multi-tiered filtration, drug-likeness evaluation (QED) and selection of top-ranked chimeric linkers. (**B** to **D**) Chemical structures and QED scores of the designed candidates: (B) CRTAP-PROTAC-AI-4 (QED, 0.520), (C) CRTAP-PROTAC-AI-53 (QED, 0.503) and (D) CRTAP-PROTAC-AI-45 (QED, 0.484). (**E**) Molecular docking and binding interaction analysis of the CRTAP-thalidomide construct predicted using CB-Dock2. (**F**) Sensorgram showing the association (0 to 300 s) and dissociation (300 to 900 s) phases of thalidomide (9.375 to 300 nM; twofold serial dilution) interacting with amine-coupled CRTAP

on AR2G biosensors. Solid colored lines represent double-referenced experimental response curves; dashed black lines represent the global fit to a 1:1 Langmuir interaction model (k_a = 1.25 × 10^5 M^{-1} s^{-1}, k_d = 4.50 × 10^{-3} s^{-1}, K_D = 36.0 nM; R^2 = 0.994, χ^2 = 0.012). (**G**) Percentage cell death measured by flow cytometry in wild-type (CRTAP-WT) and knockout (CRTAP-KO) U87MG cells following treatment with the thalidomide-based construct; **P < 0.01 by two-tailed unpaired Student's t test.

Candidate ID	Canonical SMILES String	QED Score	Molecular Weight (Da)
CRTAP-PROTAC-AI-4	CC(=O)NC(CC(C)C)C(=O)O.CCCC.O=C1CCC(N2C(=O)c3ccccc3C2=O)C(=O)N1	0.520	489.25
CRTAP-PROTAC-AI-53	CC(=O)NC(CC(C)C)C(=O)O.CCOC.O=C1CCC(N2C(=O)c3ccccc3C2=O)C(=O)N1	0.503	491.23
CRTAP-PROTAC-AI-45	CC(=O)NC(CC(C)C)C(=O)O.CCCCC.O=C1CCC(N2C(=O)c3ccccc3C2=O)C(=O)N1	0.484	503.26

Table 1: List of PROTACs predicted by generative AI pipeline

DISCUSSION

The importance of the tumor microenvironment in GBM has become increasingly recognized. Although the normal brain is relatively poor in fibrillar collagen, malignant transformation is accompanied by extensive remodeling of ECM composition and architecture, including increased deposition of extracellular proteins, altered matrix organization and changes in tissue mechanical properties (*13, 16*). These alterations influence tumor invasion, proliferation, stem-like properties and treatment response. Glioma cells actively sense and respond to their physical environment, with matrix stiffness regulating migration, proliferation and cellular phenotype through mechanotransduction pathways (*17*). More broadly, work across multiple cancer types has established that increased ECM rigidity promotes malignant progression by enhancing integrin signaling, cytoskeletal tension and downstream oncogenic pathways (*29, 31*). Our findings extend this concept by identifying CRTAP-dependent collagen maturation as a molecular mechanism contributing to the mechanical phenotype of GBM.

The observation that CRTAP depletion reduces collagen fiber organization and matrix stiffness indicates that collagen quality, and not only collagen quantity, is a determinant of the GBM microenvironment. Similar principles have been demonstrated in other malignancies, where enzymatic modification and organization of collagen fibers determine tissue mechanics and influence tumor progression. LOX-mediated collagen crosslinking increases ECM stiffness and promotes integrin-dependent signaling, invasion and metastatic dissemination in breast cancer models (*29, 30*), and collagen alignment and matrix remodeling have been associated with invasive tumor phenotypes and poor clinical outcomes in several solid tumors (*32, 34*). Whereas those studies focused on covalent crosslinking of assembled fibrils, our findings reveal an additional and earlier regulatory layer, in which the quality of the collagen molecule itself — set by prolyl 3-hydroxylation through the CRTAP-containing complex — influences tumor-associated biomechanics. This is consistent with the connective-tissue phenotype of CRTAP loss in osteogenesis imperfecta, where defective 3-hydroxylation compromises matrix mechanical strength (*27, 28*), and suggests that tumors co-opt a developmental collagen-maturation program to build a stiff niche.

A central mechanistic finding of this study is the relationship between CRTAP-dependent matrix remodeling and YAP localization. YAP and TAZ are transcriptional co-activators that function as major sensors of extracellular mechanical cues; matrix stiffness regulates their nuclear localization and transcriptional activity, establishing a direct connection between ECM mechanics and gene regulation (*23*). Subsequent work has shown that YAP and TAZ integrate signals derived from integrins, focal adhesions, actomyosin contractility and cytoskeletal tension to regulate proliferation, survival and invasion (*24–26*). In GBM, activation of mechanotransduction pathways has been implicated in maintaining aggressive tumor phenotypes, although the upstream mechanisms controlling ECM-driven YAP activation remain incompletely defined. Our data position CRTAP upstream of this pathway by showing that loss of CRTAP reduces matrix stiffness and attenuates YAP nuclear localization. Because YAP-dependent transcriptional programs themselves induce ECM regulators such as connective tissue growth factor (CTGF) and cysteine-rich angiogenic inducer 61 (CYR61), the CRTAP–collagen–YAP relationship we describe is plausibly a feed-forward loop in which mechanical signaling promotes further matrix remodeling (*25*).

The relationship between ECM remodeling and cancer progression is particularly relevant in glioblastoma, where tumor cells exhibit remarkable adaptability and resistance to therapeutic stress. Despite improvements in molecular classification and treatment strategies, TMZ resistance remains a major obstacle; established mechanisms include increased DNA repair capacity mediated by O^6-methylguanine-DNA methyltransferase (MGMT), alterations in apoptotic signaling, tumor cell heterogeneity and the persistence of therapy-resistant stem-like populations (*1, 49, 50*). These mechanisms operate within a microenvironmental context in which extracellular signals influence tumor cell survival and treatment response: matrix stiffness enhances integrin signaling and activates downstream survival pathways, including PI3K-AKT and MAPK signaling, which can blunt apoptotic responses after anticancer treatment, and mechanically altered ECM environments promote treatment resistance in breast and pancreatic cancer models (*14, 29*). Our identification of CRTAP as a determinant of GBM matrix stiffness therefore raises the testable hypothesis that CRTAP-dependent mechanical signaling contributes to the survival phenotype of GBM cells under chemotherapy, and provides a rationale for evaluating CRTAP-directed agents as sensitizers in combination with standard chemotherapy.

From a therapeutic perspective, targeting ECM mechanics is an emerging but challenging strategy. Unlike classical oncogenic drivers, ECM regulators influence both malignant cells and normal tissue architecture, raising concerns regarding toxicity and tissue homeostasis; CRTAP in particular is essential for skeletal collagen maturation, so systemic inhibition would be expected to carry bone-related liabilities (*27, 28*). Nevertheless, tumor-associated ECM remodeling may create selective vulnerabilities, because malignant cells become dependent on mechanically altered niches that sustain invasion and survival. Previous attempts to target ECM-associated pathways, including LOX inhibition, have demonstrated that altering tumor mechanics can influence disease progression, although clinical translation remains complex (*30*). Targeted protein degradation offers a route to tissue- and dose-controlled modulation that is difficult to achieve with occupancy-based inhibitors (*37*), and our generative design work is intended as a first step toward such reagents rather than as a completed therapeutic campaign.

Our study also raises broader questions regarding the interaction between tumor cell-derived ECM remodeling and the multicellular glioblastoma ecosystem. GBM progression is shaped by reciprocal communication between malignant cells and non-neoplastic populations, including

astrocytes, microglia, endothelial cells, stromal fibroblast-like cells and immune infiltrates (*16, 51*). Single-cell transcriptomic studies have revealed extensive cellular heterogeneity within GBM, with distinct tumor and microenvironmental states contributing to invasion, immune modulation and therapeutic resistance (*9, 10*). Because ECM composition and mechanical properties are likely influenced by multiple cellular populations, future investigations using spatial transcriptomics, multiplex imaging and patient-derived organoid models will be necessary to define how CRTAP-mediated remodeling integrates with the broader tumor ecosystem.

Several limitations of this study should be acknowledged. The functional experiments were performed in a single established glioblastoma line, U87MG, whose provenance has been debated; confirmation in additional lines and in patient-derived glioma stem cell models, together with in vivo orthotopic validation, will be required before the CRTAP-collagen-YAP axis can be considered general. Our survival analyses are retrospective, single-cohort and univariable, and establishing CRTAP as an independent prognostic factor will require multivariable modeling adjusted for age, grade, IDH status and MGMT promoter methylation, with validation in an independent cohort. The relationship between matrix stiffness and YAP localization reported here is correlative; direct causality would be best tested by restoring stiffness in CRTAP-null cultures on tunable substrates. Finally, the chemical work is computational and biophysical: binding and target-dependent cytotoxicity are demonstrated, but degradation of CRTAP protein, cereblon dependence and selectivity are not, and the designed molecules should accordingly be regarded as candidate degraders awaiting synthesis and validation.

Cancer progression is driven not only by genetic alterations within tumor cells but also by dynamic interactions between malignant cells and their physical environment (*52, 53*). Our work extends this paradigm by identifying a collagen-processing protein as an upstream regulator of the mechanical state of the GBM microenvironment. In conclusion, this study identifies CRTAP as a regulator of collagen-dependent ECM remodeling in glioblastoma and demonstrates that the mechanical properties of the tumor microenvironment are important determinants of malignant behavior. The CRTAP-collagen-YAP axis provides a mechanistic framework linking extracellular matrix maturation with intracellular signaling, and suggests that targeting

pathological ECM remodeling may represent a complementary strategy for overcoming the adaptive capacity of glioblastoma.

MATERIALS AND METHODS

Cell culture and transfection

U87MG and HEK293T cell lines were obtained from the National Centre for Cell Science (NCCS), Pune, India, and were cultured in Dulbecco's modified Eagle's medium (DMEM; AL068A-500ML, HiMedia) supplemented with 10% (v/v) fetal bovine serum (FBS; RM9955-500ML, HiMedia), 100 U/ml penicillin and 100 µg/ml streptomycin at 37°C in a humidified atmosphere containing 5% CO_2. NIH3T3 cells were maintained under the same conditions. Transfection of plasmid DNA into HEK293T cells in Ex-Cell medium (14366C-1000ML, Sigma-Aldrich) was performed using polyethylenimine (Sigma-Aldrich) according to the manufacturer's protocol. All lines were tested for mycoplasma and authenticated by short tandem repeat profiling

CGGA data acquisition and cohort selection

Transcriptomic expression profiles and matched clinical metadata were retrieved from the CGGA portal (http://www.cgga.org.cn) (*41*). Datasets encompassing RNA sequencing (mRNAseq_325 and mRNAseq_693) and microarray profiles (mRNA-array_301) were evaluated; the analyses reported in Figs. 1 and 2 were performed on the mRNAseq_325 dataset Clinical parameters extracted included overall survival time, vital status, histological grade, age, sex, IDH1/2 mutation status and 1p/19q codeletion status. Samples with complete survival and transcriptomic data were included in downstream quantitative analyses.

CRTAP expression profiling and clinical stratification

Normalized expression values for CRTAP were extracted from the cohort datasets and evaluated across WHO histological grades (II, III and IV) and molecular subtypes (IDH-wild-type versus IDH-mutant; 1p/19q-codeleted versus non-codeleted). For prognostic evaluation, patients were stratified into CRTAP-high and CRTAP-low groups at the median CRTAP expression value.

Overall survival curves were constructed by the Kaplan–Meier method and compared using the two-sided log-rank test.

RNA extraction and RT-qPCR

Total RNA was isolated using TRIzol reagent (Invitrogen) according to the manufacturer's instructions. RNA concentration and purity were measured on a NanoDrop 2000 spectrophotometer ($A_{260}/A_{280} \geq 1.9$) and integrity was validated on an Agilent 2100 Bioanalyzer (RNA integrity number ≥ 8.0). For complementary DNA synthesis, 1.0 μg of genomic DNA-depleted total RNA was reverse-transcribed using the High-Capacity cDNA Reverse Transcription Kit (Applied Biosystems). Quantitative real-time PCR was performed on a Bio-Rad CFX Opus 96 instrument using PowerUp SYBR Green Master Mix (Thermo Fisher Scientific) under standard thermal parameters (95°C for 2 min, followed by 40 cycles of 95°C for 15 s and 60°C for 60 s). Single-product specificity was confirmed by post-amplification melt-curve analysis. Relative expression was quantified using the comparative $2^{-\Delta\Delta C_\{T\}}$ method with normalization to GAPDH across three independent biological replicates (n = 3). Primer sequences are listed in table.

Immunohistochemistry and tissue microarray analysis

Glioma tissue microarrays were obtained from US Biomax/TissueArray.com and processed for immunohistochemical staining. Slides were deparaffinized in xylene and rehydrated through a graded ethanol series. Heat-induced epitope retrieval was performed in 10 mM sodium citrate buffer (pH 6.0) at 95°C for 20 min. Endogenous peroxidase activity was quenched with 3% H_2O_2 in methanol for 10 min, followed by blocking in 5% normal goat serum in phosphate-buffered saline (PBS) for 1 hour at room temperature. Slides were incubated overnight at 4°C with a primary antibody against CRTAP, followed by horseradish peroxidase-conjugated secondary antibody for 1 hour at room temperature. Chromogenic signal was developed using DAB substrate and sections were counterstained with hematoxylin. High-resolution digital slide scanning was performed on a Leica DMi8 microscope (*42*).

Lentiviral CRISPR-Cas9 mediated gene knockout and rescue

Single-guide RNAs targeting human CRTAP were designed using the Benchling CRISPR design tool and cloned into lentiCRISPRv2 (Addgene plasmid no. 52961) (*43*). Lentiviral particles were generated by co-transfecting HEK293T cells with lentiCRISPRv2 carrying the target sgRNA, the packaging plasmid psPAX2 (Addgene no. 12260) and the envelope plasmid pMD2.G (Addgene no. 12259) at a 4:3:1 molar ratio using Lipofectamine 3000 (Thermo Fisher Scientific). Viral supernatants were harvested at 48 and 72 hours after transfection, cleared of debris by 0.45-μm polyvinylidene difluoride filtration and concentrated using PEG-it virus precipitation solution. U87MG target cells were transduced in the presence of 8 μg/ml polybrene for 24 hours and selected under puromycin (2 μg/ml) for 7 days. Single-cell clones were isolated by limiting dilution in 96-well plates. Knockout efficiency was validated by Sanger sequencing of the target locus and by RT-qPCR.

Cell proliferation assay

Cell viability and proliferation of wild-type, knockout and rescue cells were evaluated using the 3-(4,5-dimethylthiazol-2-yl)-2,5-diphenyltetrazolium bromide (MTT) colorimetric assay. Cells were seeded into 96-well plates at 3×10^3 cells per well in 100 μl of complete growth medium and allowed to adhere overnight. Proliferation was monitored over a 5-day time course at 24-hour intervals (24, 48, 72, 96 and 120 hours). At each time point, 10 μl of MTT reagent (5 mg/ml in PBS; Sigma-Aldrich) was added to each well and incubated at 37°C for 4 hours. Formazan crystals were dissolved by replacing the medium with 150 μl of dimethyl sulfoxide per well followed by gentle agitation for 10 min, and absorbance was measured at 570 nm (reference wavelength, 630 nm) on a microplate reader. Assays were conducted in triplicate across three independent biological experiments (n = 3).

Clonogenic survival assay

Wild-type, knockout and rescue cells were harvested, resuspended as single cells and seeded into six-well plates at 500 cells per well in complete growth medium. Plates were incubated at 37°C under 5% CO_2 for 14 days to allow colony formation, with medium refreshed every 3 days. The medium was then aspirated and wells were washed twice with ice-cold PBS. Colonies were fixed with 4% paraformaldehyde in PBS for 15 min at room temperature and stained with 0.5% (w/v)

crystal violet in 20% methanol for 30 min. Excess stain was removed by rinsing under running tap water and plates were air-dried. Images of stained colonies were captured on a Leica DMi8 microscope and colonies were counted automatically in ImageJ/Fiji (*42*). Colonies were counted across three independent biological experiments conducted in triplicate (n = 3).

Three dimensional spheroid invasion assay

Tumor spheroid formation and three-dimensional matrix invasion were evaluated using hanging drop method with Matrigel embedding. Single-cell suspensions of wild-type, knockout and rescue cells were seeded at 2×10^3 cells per well in 96-well round-bottom ULA plates (Corning) and cultured for 48 to 72 hours to allow compact spheroid assembly. Subsequently, 50 µl of culture medium was gently removed from each well and replaced with 50 µl of ice-cold growth factor-reduced Matrigel (Corning; final concentration ≈ 4.5 mg/ml) supplemented with collagen I (0.5 mg/ml). Plates were incubated at 37°C for 1 hour to allow matrix gelation before addition of 100 µl of complete growth medium. Spheroid invasion was monitored by bright-field microscopy at 0, 24, 48 and 72 hours after embedding. The total area occupied by the spheroid and its invasive sprouts was measured in ImageJ/Fiji (*42*) and is reported in Fig. 3F as the absolute invaded area in μm^2. Assays were performed in biological triplicate with at least six spheroids per condition (n = 3).

Ascorbate-stimulated ECM deposition and collagen I purification

To stimulate ECM production and collagen maturation, cultures were grown to confluence and the medium was supplemented with 50 µg/ml L-ascorbic acid, freshly replenished every 48 hours, for 14 days. Following the 2-week induction period, cell-derived collagen I was isolated and purified. Cultures were washed with ice-cold PBS and cells were removed using a hypotonic detergent buffer (0.5% Triton X-100 in PBS with protease inhibitors). The remaining insoluble ECM was washed extensively with sterile PBS. Collagen was extracted by enzymatic digestion with pepsin (1 mg/ml in 0.5 M acetic acid) at 4°C for 24 hours with constant agitation. Solubilized collagen was precipitated by adding NaCl to a final concentration of 0.9 M, collected by centrifugation (12,000g for 30 min at 4°C), redissolved in 0.5 M acetic acid and dialyzed extensively against cold distilled water to remove salts.

Hydroxyproline assay

Hydroxyproline content of the purified collagen extracts was quantified using a colorimetric assay kit (MAK008, Sigma-Aldrich) following the manufacturer's protocol. Aliquots of purified collagen were transferred to pressure-safe vials, mixed with equal volumes of 6 N HCl and hydrolyzed at 110°C for 24 hours. Hydrolysates were evaporated to dryness at 60°C under vacuum. The dried residue was reconstituted in assay buffer, treated with chloramine-T oxidation buffer and incubated at room temperature for 5 min. Ehrlich's reagent (4-dimethylaminobenzaldehyde in perchloric acid and isopropanol) was then added to each well and the chromophore was developed by incubating the plate at 60°C for 90 min. Absorbance was measured at 560 nm on a microplate reader. Hydroxyproline concentrations were calculated from a standard curve constructed with trans-4-hydroxyproline reference standards and normalized to total protein.

Magnetic tweezers microrheology and matrix stiffness measurement

To quantify the micromechanical stiffness of the matrix across wild-type, CRTAP-KO and CRTAP-rescue conditions, glass coverslips were chemically activated by immersion in piranha solution for 2 hours, rinsed with distilled water and cleaned by five cycles of bath sonication. Superparamagnetic beads (100 µl) of 2.4 µm diameter were deposited onto air-dried coverslips and incubated for 1 hour at room temperature. Cells (1×10^5 cells per coverslip) were seeded onto the collagen matrix. As mentioned earlier ascorbate stimulated ECM deposition was performed. ECM secreted cells were then used for stiffness measurements. Micromechanical measurements were performed on a custom-built magnetic tweezers platform (Fig. 4B). Stiffness and extension profiles were acquired by applying a force of 100 pN. Displacement trajectories were analyzed by kernel density estimation to extract probability distributions, and data fitting and stiffness quantification were performed in OriginPro.

Masson's trichrome staining and collagen morphometry

Cell-derived ECM constructs or matrix-embedded cultures from wild-type, knockout and rescue conditions were fixed in 4% paraformaldehyde in PBS for 20 min at room temperature and

washed gently with PBS. Samples were refixed in Bouin's fluid at 56°C for 1 hour to enhance color contrast, washed under running tap water to remove excess picric acid and stained using a Masson's trichrome stain kit according to the manufacturer's instructions. Nuclei were stained with Weigert's iron hematoxylin for 10 min, followed by cytoplasmic staining with Biebrich scarlet-acid fuchsin for 15 min. Samples were differentiated in phosphomolybdic-phosphotungstic acid solution for 15 min and immediately transferred to aniline blue solution for 10 min to selectively stain collagen fibers. After a brief rinse in 1% acetic acid, samples were dehydrated through a graded ethanol series, cleared in xylene and mounted in synthetic mounting medium. Bright-field images were acquired on a Leica DMi8 microscope under uniform exposure settings. For collagen area fraction analysis, color deconvolution was performed in ImageJ/Fiji (*42*) to isolate the aniline blue channel; the thresholded collagen area was normalized to the total region of interest to derive the collagen area fraction (%). Analyses were conducted across at least three independent biological replicates (n = 3), evaluating a minimum of five random fields per condition.

Immunofluorescence confocal microscopy and N/C ratio quantification

Wild-type and knockout cells were seeded onto glass coverslips in 24-well plates, cultured for 24 hours and fixed with 4% paraformaldehyde in PBS for 15 min at room temperature. Fixed cells were washed three times with PBS, permeabilized with 0.1% Triton X-100 in PBS for 10 min and blocked with 5% bovine serum albumin (BSA) in PBS for 1 hour at room temperature. Coverslips were incubated overnight at 4°C with the primary anti-YAP antibody diluted in 1% BSA. After three PBS washes, cells were incubated with an Alexa Fluor-conjugated secondary antibody (red channel) for 1 hour at room temperature in the dark. Nuclei were counterstained with DAPI (cyan channel) for 10 min. Coverslips were mounted using antifade mounting medium and images were acquired on a Zeiss LSM 980 confocal laser scanning microscope. For quantification of the nuclear-to-cytoplasmic ratio, image analysis was performed in ImageJ/Fiji (*42*). Nuclear boundaries were defined by DAPI mask segmentation, the mean fluorescence

intensity within the nucleus ($F_{nuclear}$) and in a cytoplasmic ring adjacent to the nucleus ($F_{cytoplasmic}$) was measured for individual cells, and background intensity was subtracted. The nuclear-to-cytoplasmic ratio was calculated as $N/C = F_{nuclear}/F_{cytoplasmic}$.

Gene correlation and Gene Ontology enrichment analysis

To identify genes co-regulated with CRTAP in GBM, expression correlation analysis was performed using GEPIA2 (http://gepia2.cancer-pku.cn) (*44*). A ranked gene list was generated on the basis of the Pearson correlation coefficient between CRTAP expression and all transcriptomic profiles in the TCGA-GBM dataset. Functional annotation and pathway enrichment analyses were conducted in R. The ranked gene list was subjected to Gene Ontology enrichment analysis across Biological Process, Cellular Component and Molecular Function domains using the clusterProfiler package (v4.8.0) (*45*) with the human genome annotation database org.Hs.eg.db. Gene Set Enrichment Analysis was executed using a minimum gene set size of 10 and a maximum of 500. P values were adjusted for multiple testing using the Benjamini–Hochberg false discovery rate (FDR) procedure, and enriched terms with FDR < 0.05 were considered statistically significant. Visualization was generated using the enrichplot and ggplot2 R packages.

Generative design of CRTAP-directed chimeras

To identify structural linkers capable of bridging the thalidomide E3 ligase anchor (O=C1NC(=O)CCC1N2C(=O)c3ccccc3C2=O) and a CRTAP-directed fragment (CC(C)CC(C(=O)O)NC(=O)C), an automated computer-aided drug design pipeline was implemented using the open-source cheminformatics toolkit RDKit (v2023.03) (*46*). A stochastic genetic algorithm generated a library of linkers composed of flexible alkyl and polyethylene glycol-mimicking elements ranging from 4 to 12 atoms in length, sampling a pool of 500 distinct configurations. Fragment assembly was performed by programmatic atom mapping. Candidates were filtered using a multi-tiered mask based on Lipinski's rules, valency verification via RDKit sanitization routines and a molecular weight threshold of 1200 Da. Drug-likeness was evaluated using the quantitative estimate of drug-likeness (QED) framework (*47*) to rank the final library.

Molecular docking

Protein-ligand docking of the CRTAP-thalidomide construct was performed with the CB-Dock2 server (*48*), which combines curvature-based cavity detection with template-based docking. Binding poses were ranked by predicted binding energy and the top-scoring pose was used to identify contact residues.

Bio-layer interferometry

Real-time binding kinetics between recombinant CRTAP and thalidomide were measured on an Octet RED96 system (Sartorius) at 25°C with continuous orbital shaking at 1000 rpm. Amine-reactive second-generation (AR2G) biosensors were pre-hydrated in Milli-Q water for 10 min. Biosensor surfaces were activated for 300 s using a freshly prepared mixture of 20 mM 1-ethyl-3-(3-dimethylaminopropyl)carbodiimide and 10 mM N-hydroxysulfosuccinimide. CRTAP was diluted in 10 mM sodium acetate buffer and covalently coupled to the activated biosensors for 600 s, targeting a stable loading shift of 1.0 to 1.2 nm. Unreacted esters were quenched with 1 M ethanolamine-HCl (pH 8.5) for 300 s. Baseline equilibration was established by dipping CRTAP-functionalized biosensors into assay buffer (10 mM PBS, pH 7.4, 150 mM NaCl, 0.05% (v/v) Tween-20, 0.1% (w/v) BSA and 1% (v/v) dimethyl sulfoxide) for 120 s. Association was monitored by transferring biosensors into a twofold serial dilution series of thalidomide (9.375 to 300 nM in assay buffer) for 300 s, and dissociation was recorded in analyte-free assay buffer for 600 s. Parallel reference channels (ethanolamine-blocked AR2G biosensors without CRTAP, exposed to the thalidomide dilutions) and zero-analyte control blanks were measured simultaneously to correct for baseline drift and non-specific binding. Data were processed in Octet Data Analysis Software v12.0; double-referenced sensorgrams were aligned to the association start step and globally fitted to a 1:1 Langmuir binding model. Goodness of fit was assessed by the coefficient of determination ($R^2 > 0.98$) and the reduced chi-square value ($\chi^2 < 0.05$).

PROTAC treatment and flow cytometric quantification of cell death

Cells were seeded into 6-well tissue culture plates at a density of 2×10^5 cells per well and incubated for 24 hours to allow attachment prior to drug exposure. Thalidomide PROTAC (catalog no. DC45747) was reconstituted in sterile dimethyl sulfoxide (DMSO) to prepare a 10 mM stock solution and diluted in complete growth medium to a final working concentration of 5 μM, maintaining a uniform final DMSO vehicle concentration of $\leq 0.1\%$ (v/v) across all experimental conditions. Both CRTAP-WT and CRTAP-KO groups were treated with Thalidomide PROTAC for incubation time 48 hours at 37°C and 5% CO_2. At the experimental endpoint, floating and loosely attached cells in the culture supernatant were collected into 15 mL conical tubes, and remaining adherent cells were gently detached using 0.05% trypsin-EDTA and neutralized with complete serum-containing medium. Pooled cell suspensions from each well were centrifuged at $300g$ for 5 min at 4°C, washed once with ice-cold Dulbecco's phosphate-buffered saline (PBS, pH 7.4), and stained using the Dead Cell Apoptosis Kit with Annexin V FITC and propidium iodide (PI) (Thermo Fisher Scientific, catalog no. V13242) in accordance with the manufacturer's instructions. Specifically, cell pellets were resuspended in 100 μL of $1 \times$ annexin-binding buffer (10 mM HEPES, 140 mM NaCl, 2.5 mM $CaCl_2$, pH 7.4) at approximately 1×10^6 cells/mL, followed by the addition of 5 μL of FITC-conjugated Annexin V and 1 μL of 100 μg/mL PI working solution. Samples were gently mixed and incubated for 15 min at room temperature in the dark, after which 400 μL of ice-cold $1 \times$ annexin-binding buffer was added to each tube prior to immediate flow cytometric acquisition. Data acquisition was performed on a BD FACSAria flow cytometer (BD Biosciences) equipped with a 488 nm blue excitation laser, detecting Annexin V-FITC emission using a 530/30 nm bandpass filter and PI emission using a 616/23 nm bandpass filter. Unstained cells and single stained compensation controls (Annexin V-FITC only and PI only) were used to calibrate photomultiplier tube (PMT) voltages and establish fluorescence spillover compensation matrices in BD FACSDiva software (BD Biosciences). A minimum of 10,000 single cell events per sample were recorded after excluding cellular debris via forward scatter area versus side scatter area gating and excluding cell doublets via forward scatter height versus forward scatter width gating. Flow cytometric data were analyzed using FlowJo v10. Quadrant gates defined on vehicle-treated controls partitioned cells into viable ($\text{Annexin V}^-/\text{PI}^-$), early apoptotic ($\text{Annexin V}^+/\text{PI}^-$), late apoptotic ($\text{Annexin V}^+/\text{PI}^+$), and necrotic ($\text{Annexin V}^-/\text{PI}^+$) fractions, with total percentage cell death (% Cell Death) calculated as the cumulative sum of all Annexin V^+ and/or PI^+ populations.

Statistical analysis

All statistical analyses and survival visualizations were performed in GraphPad Prism (v9.0). Continuous variables between two groups were compared using the two-tailed unpaired Student's t test or the Mann–Whitney U test as appropriate; comparisons across more than two groups used one-way or two-way analysis of variance with Tukey's post hoc test; categorical parameters were compared using the χ^2 test; and survival distributions were compared using the two-sided log-rank test. Unless stated otherwise, data are presented as box-and-whisker plots showing the median and interquartile range, or as mean ± SD, from three independent biological experiments. Statistical significance was defined as $P < 0.05$ (*$P < 0.05$, $P < 0.01$,* **$P < 0.001$).

REFERENCES

1. R. Stupp, W. P. Mason, M. J. van den Bent, M. Weller, B. Fisher, M. J. B. Taphoorn, et al., Radiotherapy plus concomitant and adjuvant temozolomide for glioblastoma. *N. Engl. J. Med.* **352**, 987–996 (2005).

2. R. Stupp, M. E. Hegi, W. P. Mason, M. J. van den Bent, M. J. B. Taphoorn, R. C. Janzer, et al., Effects of radiotherapy with concomitant and adjuvant temozolomide versus radiotherapy alone on survival in glioblastoma in a randomised phase III study: 5-year analysis of the EORTC-NCIC trial. *Lancet Oncol.* **10**, 459–466 (2009).

3. M. Weller, M. van den Bent, M. Preusser, E. Le Rhun, J. C. Tonn, G. Minniti, et al., EANO guidelines on the diagnosis and treatment of diffuse gliomas of adulthood. *Nat. Rev. Clin. Oncol.* **18**, 170–186 (2021).

4. D. N. Louis, A. Perry, P. Wesseling, D. J. Brat, I. A. Cree, D. Figarella-Branger, et al., The 2021 WHO Classification of Tumors of the Central Nervous System: A summary. *Neuro Oncol.* **23**, 1231–1251 (2021).

5. The Cancer Genome Atlas Research Network, Comprehensive genomic characterization defines human glioblastoma genes and core pathways. *Nature* **455**, 1061–1068 (2008).

6. R. G. W. Verhaak, K. A. Hoadley, E. Purdom, V. Wang, Y. Qi, M. D. Wilkerson, et al., Integrated genomic analysis identifies clinically relevant subtypes of glioblastoma characterized by abnormalities in PDGFRA, IDH1, EGFR, and NF1. *Cancer Cell* **17**, 98–110 (2010).

7. C. W. Brennan, R. G. W. Verhaak, A. McKenna, B. Campos, H. Noushmehr, S. R. Salama, et al., The somatic genomic landscape of glioblastoma. *Cell* **155**, 462–477 (2013).

8. M. Ceccarelli, F. P. Barthel, T. M. Malta, T. S. Sabedot, S. R. Salama, B. A. Murray, et al., Molecular profiling reveals biologically discrete subsets and pathways of progression in diffuse glioma. *Cell* **164**, 550–563 (2016).

9. A. P. Patel, I. Tirosh, J. J. Trombetta, A. K. Shalek, S. M. Gillespie, H. Wakimoto, et al., Single-cell RNA-seq highlights intratumoral heterogeneity in primary glioblastoma. *Science* **344**, 1396–1401 (2014).

10. C. Neftel, J. Laffy, M. G. Filbin, T. Hara, M. E. Shore, G. J. Rahme, et al., An integrative model of cellular states, plasticity, and genetics for glioblastoma. *Cell* **178**, 835–849.e21 (2019).

11. R. O. Hynes, The extracellular matrix: Not just pretty fibrils. *Science* **326**, 1216–1219 (2009).

12. C. Frantz, K. M. Stewart, V. M. Weaver, The extracellular matrix at a glance. *J. Cell Sci.* **123**, 4195–4200 (2010).

13. P. Lu, V. M. Weaver, Z. Werb, The extracellular matrix: A dynamic niche in cancer progression. *J. Cell Biol.* **196**, 395–406 (2012).

14. M. W. Pickup, J. K. Mouw, V. M. Weaver, The extracellular matrix modulates the hallmarks of cancer. *EMBO Rep.* **15**, 1243–1253 (2014).

15. T. R. Cox, J. T. Erler, Remodeling and homeostasis of the extracellular matrix: Implications for fibrotic diseases and cancer. *Dis. Model. Mech.* **4**, 165–178 (2011).

16. D. F. Quail, J. A. Joyce, The microenvironmental landscape of brain tumors. *Cancer Cell* **31**, 326–341 (2017).

17. T. A. Ulrich, E. M. de Juan Pardo, S. Kumar, The mechanical rigidity of the extracellular matrix regulates the structure, motility, and proliferation of glioma cells. *Cancer Res.* **69**, 4167–4174 (2009).

18. D. E. Discher, P. Janmey, Y.-L. Wang, Tissue cells feel and respond to the stiffness of their substrate. *Science* **310**, 1139–1143 (2005).

19. A. J. Engler, S. Sen, H. L. Sweeney, D. E. Discher, Matrix elasticity directs stem cell lineage specification. *Cell* **126**, 677–689 (2006).

20. V. Vogel, M. Sheetz, Local force and geometry sensing regulate cell functions. *Nat. Rev. Mol. Cell Biol.* **7**, 265–275 (2006).

21. G. Charras, E. Sahai, Physical influences of the extracellular environment on cell migration. *Nat. Rev. Mol. Cell Biol.* **15**, 813–824 (2014).

22. D. E. Jaalouk, J. Lammerding, Mechanotransduction gone awry. *Nat. Rev. Mol. Cell Biol.* **10**, 63–73 (2009).

23. S. Dupont, L. Morsut, M. Aragona, E. Enzo, S. Giulitti, M. Cordenonsi, et al., Role of YAP/TAZ in mechanotransduction. *Nature* **474**, 179–183 (2011).

24. S. Piccolo, S. Dupont, M. Cordenonsi, The biology of YAP/TAZ: Hippo signaling and beyond. *Physiol. Rev.* **94**, 1287–1312 (2014).

25. F. Zanconato, M. Cordenonsi, S. Piccolo, YAP/TAZ at the roots of cancer. *Cancer Cell* **29**, 783–803 (2016).

26. T. Panciera, L. Azzolin, M. Cordenonsi, S. Piccolo, Mechanobiology of YAP and TAZ in physiology and disease. *Nat. Rev. Mol. Cell Biol.* **18**, 758–770 (2017).

27. R. Morello, T. K. Bertin, Y. Chen, J. Hicks, L. Tonachini, M. Monticone, et al., CRTAP is required for prolyl 3-hydroxylation and mutations cause recessive osteogenesis imperfecta. *Cell* **127**, 291–304 (2006).

28. W. A. Cabral, A. M. Barnes, E. Abernathy, M. Weis, M. Chang, D. R. Eyre, et al., Prolyl 3-hydroxylase 1 deficiency causes a recessive metabolic bone disorder resembling lethal/severe osteogenesis imperfecta. *Nat. Genet.* **39**, 359–365 (2007).

29. K. R. Levental, H. Yu, L. Kass, J. N. Lakins, M. Egeblad, J. T. Erler, et al., Matrix crosslinking forces tumor progression by enhancing integrin signaling. *Cell* **139**, 891–906 (2009).

30. T. R. Cox, D. Bird, A.-M. Baker, H. E. Barker, M. W.-Y. Ho, G. Lang, J. T. Erler, LOX-mediated collagen crosslinking is responsible for fibrosis-enhanced metastasis. *Cancer Res.* **73**, 1721–1732 (2013).

31. M. J. Paszek, N. Zahir, K. R. Johnson, J. N. Lakins, G. I. Rozenberg, A. Gefen, et al., Tensional homeostasis and the malignant phenotype. *Cancer Cell* **8**, 241–254 (2005).

32. P. P. Provenzano, K. W. Eliceiri, J. M. Campbell, D. R. Inman, J. G. White, P. J. Keely, Collagen reorganization at the tumor-stromal interface facilitates local invasion. *BMC Med.* **6**, 11 (2008).

33. P. Friedl, K. Wolf, Tumour-cell invasion and migration: Diversity and escape mechanisms. *Nat. Rev. Cancer* **3**, 362–374 (2003).

34. P. Friedl, S. Alexander, Cancer invasion and the microenvironment: Plasticity and reciprocity. *Cell* **147**, 992–1009 (2011).

35. S. Kumar, V. M. Weaver, Mechanics, malignancy, and metastasis: The force journey of a tumor cell. *Cancer Metastasis Rev.* **28**, 113–127 (2009).

36. K. M. Sakamoto, K. B. Kim, A. Kumagai, F. Mercurio, C. M. Crews, R. J. Deshaies, Protacs: Chimeric molecules that target proteins to the Skp1–Cullin–F box complex for ubiquitination and degradation. *Proc. Natl. Acad. Sci. U.S.A.* **98**, 8554–8559 (2001).

37. M. Békés, D. R. Langley, C. M. Crews, PROTAC targeted protein degraders: The past is prologue. *Nat. Rev. Drug Discov.* **21**, 181–200 (2022).

38. T. Ito, H. Ando, T. Suzuki, T. Ogura, K. Hotta, Y. Imamura, Y. Yamaguchi, H. Handa, Identification of a primary target of thalidomide teratogenicity. *Science* **327**, 1345–1350 (2010).

39. A. Zhavoronkov, Y. A. Ivanenkov, A. Aliper, M. S. Veselov, V. A. Aladinskiy, A. V. Aladinskaya, et al., Deep learning enables rapid identification of potent DDR1 kinase inhibitors. *Nat. Biotechnol.* **37**, 1038–1040 (2019).

40. J. M. Stokes, K. Yang, K. Swanson, W. Jin, A. Cubillos-Ruiz, N. M. Donghia, et al., A deep learning approach to antibiotic discovery. *Cell* **180**, 688–702.e13 (2020).

41. Z. Zhao, K.-N. Zhang, Q. Wang, G. Li, F. Zeng, Y. Zhang, et al., Chinese Glioma Genome Atlas (CGGA): A comprehensive resource with functional genomic data from Chinese glioma patients. *Genomics Proteomics Bioinformatics* **19**, 1–12 (2021).

42. J. Schindelin, I. Arganda-Carreras, E. Frise, V. Kaynig, M. Longair, T. Pietzsch, et al., Fiji: An open-source platform for biological-image analysis. *Nat. Methods* **9**, 676–682 (2012).

43. N. E. Sanjana, O. Shalem, F. Zhang, Improved vectors and genome-wide libraries for CRISPR screening. *Nat. Methods* **11**, 783–784 (2014).

44. Z. Tang, B. Kang, C. Li, T. Chen, Z. Zhang, GEPIA2: An enhanced web server for large-scale expression profiling and interactive analysis. *Nucleic Acids Res.* **47**, W556–W560 (2019).

45. T. Wu, E. Hu, S. Xu, M. Chen, P. Guo, Z. Dai, et al., clusterProfiler 4.0: A universal enrichment tool for interpreting omics data. *Innovation* **2**, 100141 (2021).

46. RDKit: Open-source cheminformatics; https://www.rdkit.org.

47. G. R. Bickerton, G. V. Paolini, J. Besnard, S. Muresan, A. L. Hopkins, Quantifying the chemical beauty of drugs. *Nat. Chem.* **4**, 90–98 (2012).

48. Y. Liu, X. Yang, J. Gan, S. Chen, Z.-X. Xiao, Y. Cao, CB-Dock2: Improved protein–ligand blind docking by integrating cavity detection, docking and homologous template fitting. *Nucleic Acids Res.* **50**, W159–W164 (2022).

49. M. E. Hegi, A.-C. Diserens, T. Gorlia, M.-F. Hamou, N. de Tribolet, M. Weller, et al., MGMT gene silencing and benefit from temozolomide in glioblastoma. *N. Engl. J. Med.* **352**, 997–1003 (2005).

50. S. Bao, Q. Wu, R. E. McLendon, Y. Hao, Q. Shi, A. B. Hjelmeland, M. W. Dewhirst, D. D. Bigner, J. N. Rich, Glioma stem cells promote radioresistance by preferential activation of the DNA damage response. *Nature* **444**, 756–760 (2006).

51. R. Kalluri, M. Zeisberg, Fibroblasts in cancer. *Nat. Rev. Cancer* **6**, 392–401 (2006).

52. D. Hanahan, R. A. Weinberg, Hallmarks of cancer: The next generation. *Cell* **144**, 646–674 (2011).

53. D. Hanahan, Hallmarks of cancer: New dimensions. *Cancer Discov.* **12**, 31–46 (2022).

Acknowledgments

We thank the Department of Biological Sciences, IISER Mohali, for access to the super-resolution confocal microscopy facility.

Funding:

D.S. and P.S. acknowledge fellowship support from the Council of Scientific and Industrial Research (CSIR), India. This work was supported by institutional funds from IISER Mohali.

Author contributions:

Conceptualization: S.R. and D.S. Methodology: D.S. and P.S. Investigation: D.S. performed the cell culture, molecular, histological and computational experiments; P.S. performed and analyzed the magnetic tweezers experiments. Formal analysis: D.S. and P.S. Visualization: D.S. Supervision: S.R. Funding acquisition: S.R. Writing – original draft: D.S. Writing – review and editing: D.S. and S.R.

Competing interests:

The authors declare that they have no competing interests.

Data and materials availability:

All data needed to evaluate the conclusions in the paper are present in the paper and/or the Supplementary Materials. The code for the generative design pipeline will be deposited in a public repository (GitHub) with a citable DOI upon publication.